

OneFlowSBI: One Model, Many Queries for Simulation-Based Inference

Mayank Nautiyal^{1,2} Li Ju^{1,2}
 Melker Ernfors¹ Klara Hagland¹ Ville Holma¹ Maximilian Werkö Söderholm¹
 Andreas Hellander¹ Prashant Singh^{1,2}

Abstract

We introduce *OneFlowSBI*, a unified framework for simulation-based inference that learns a single flow-matching generative model over the joint distribution of parameters and observations. Leveraging a query-aware masking distribution during training, the same model supports multiple inference tasks, including posterior sampling, likelihood estimation, and arbitrary conditional distributions, without task-specific retraining. We evaluate *OneFlowSBI* on ten benchmark inference problems and two high-dimensional real-world inverse problems across multiple simulation budgets. *OneFlowSBI* is shown to deliver competitive performance against state-of-the-art generalized inference solvers and specialized posterior estimators, while enabling efficient sampling with few ODE integration steps and remaining robust under noisy and partially observed data.

1. Introduction

Mechanistic models and simulators are indispensable tools that complement theoretical and experimental science, enabling a deeper understanding of physical systems and accelerating scientific discovery. Simulation-based inference (SBI) has gained increasing prominence recently in various domains such as systems biology, epidemiology, physics, and climate science, as means to fit observed data to simulators (Cranmer et al., 2020). Once calibrated in this way, the simulators can be used to evaluate *what-if* scenarios, or explore various behaviors present in the underlying physical system. However, high-fidelity simulators are often characterized by significant complexity, rendering the model likelihood either analytically intractable or computationally prohibitive to evaluate. Because the likeli-

hood is frequently defined implicitly through marginalization over unobserved latent variables (Lavin et al., 2021), classical likelihood-based inference methods become impractical. SBI addresses this by learning surrogate models from samples $(\theta, \mathbf{y}) \sim p(\theta)p(\mathbf{y} | \theta)$, where $p(\theta)$ is a user defined prior encoding domain knowledge or plausibility constraints, and $p(\mathbf{y} | \theta)$ is accessed only through simulator calls, without explicit likelihood evaluation (Sisson et al., 2018). These learned surrogates are then used within Bayesian inference pipelines to approximate a range of inference targets, including posterior distributions, likelihood functions, marginal estimates, and conditional distributions, under limited simulation budgets.

Most existing SBI methods are designed as specialized solvers for a single inference target, commonly the posterior, using expressive conditional generative models (Greenberg et al., 2019; Papamakarios & Murray, 2016; Ramesh et al., 2022; Geffner et al., 2023; Wildberger et al., 2023). While effective for standard posterior inference, this paradigm becomes restrictive in generalized settings where observations may be missing, partially observed, or corrupted by measurement noise, and where downstream workflows require access beyond the full posterior – such as likelihood surrogates for model criticism (Radev et al., 2023). These considerations motivate learning a reusable representation of the joint distribution $p(\theta, \mathbf{y})$ that supports flexible conditional queries (Gloeckler et al., 2024). However, learning the full joint distribution is substantially more challenging than learning the posterior alone, particularly when the parameter space is low-dimensional but the observations are high-dimensional (e.g., time-series/spatiotemporal modeling). This difficulty is further amplified by modality mismatch, where the structural disparity between vector-valued parameters and structured observations (e.g., images or trajectories) makes scalable joint modeling non-trivial.

To address these challenges of dimensionality and modality mismatch in the generalized inference setting, we introduce a unified framework that learns a single generative model of the joint distribution $p(\theta, \mathbf{y})$ via flow matching. Leveraging a stable regression objective rooted in optimal transport geometry, the proposed *OneFlowSBI* framework effectively bridges the structural gap between parameters and

¹ Department of Information Technology, Uppsala University, Uppsala, Sweden ² Science for Life Laboratory, Uppsala University, Uppsala, Sweden . Correspondence to: Mayank Nautiyal <mayank.nautiyal@it.uu.se>.

high-dimensional observations and supports efficient sampling through favorable flow geometry. This approach utilizes dynamic coordinate masking to enable a single trained model to answer a wide range of inference queries, including posterior estimation, likelihood evaluation, and arbitrary conditionals—without retraining. Empirically, *OneFlowSBI* closely matches or exceeds specialized methods across a majority of benchmarks and simulation budgets while retaining full generality, specifically outperforming baselines on complex multimodal distributions.

Contributions. (i) We introduce *OneFlowSBI*, a unified joint flow-matching framework that enables diverse inferential queries within a single, masked generative model.

(ii) We derive a mask-aware flow formulation using linear probability paths that enforce straight transport geometry; enabling high-fidelity conditional sampling with minimal ODE discretization overhead.

(iii) The proposed framework is empirically validated on ten benchmark problems with varying structural and statistical difficulty, together with two high-dimensional inverse problems, demonstrating competitive accuracy and robustness under noisy and partially observed data.

Outline. Section 2 reviews related work. Section 3 introduces the preliminaries. Section 4 presents the proposed method. Results and ablations are reported in Sections 5 and 6. Section 7 concludes the paper.

2. Related Work

The related literature is organized into three broad categories, covering specialized posterior solvers, likelihood-based SBI approaches, and generalized SBI frameworks.

Specialized posterior solvers. A large body of neural SBI work focuses on learning the posterior $p(\theta | \mathbf{y})$ directly from simulated pairs $\{(\theta_i, \mathbf{y}_i)\}_{i=1}^N$ using expressive conditional generative models. A notable advantage is amortization: once trained, the model provides posterior inference for any new observation via a single forward pass, eliminating the need for per-instance optimization. This contrasts starkly with classical likelihood-free methods such as Approximate Bayesian Computation (ABC) (Beaumont et al., 2002) and Sequential Monte Carlo ABC (SMC-ABC) (Toni et al., 2009), which require repeated simulation with acceptance or weighting schemes, hand-crafted summary statistics, and distance metrics that may scale poorly to high-dimensional observations (Sisson et al., 2018).

Neural posterior estimation (NPE) is an early amortized posterior inference approach, learning a conditional density $q_\psi(\theta | \mathbf{y})$ from simulations for fast posterior sampling (Papamakarios & Murray, 2016). Sequential variants improve inference performance at a fixed simulation budget by iter-

atively refining the estimator and concentrating simulations in regions of high posterior mass (Papamakarios & Murray, 2016; Lueckmann et al., 2017; Greenberg et al., 2019). Beyond normalizing flows, posterior inference has been explored with adversarial training (Ramesh et al., 2022) and continuous-time methods such as flow matching posterior estimation (FMPE), which learns conditional vector fields via flow matching objectives (Wildberger et al., 2023). Despite strong empirical performance, these methods specialize to $p(\theta | \mathbf{y})$ and do not readily support alternative inference queries, missing observations, or corrupted data without retraining or additional inference mechanisms.

Likelihood-based solvers. A complementary approach targets the simulator likelihood rather than the posterior. Neural likelihood estimation (NLE) trains a conditional density model $q_\psi(\mathbf{y} | \theta) \approx p(\mathbf{y} | \theta)$ by maximizing its conditional log-likelihood on simulated pairs, typically using normalizing flows as flexible likelihood surrogates (Cranmer et al., 2020). This separation is attractive because a learned likelihood can be reused across priors and supports downstream Bayesian queries beyond posterior sampling. However, in practice, posterior inference requires additional MCMC steps to draw samples, introducing computational overhead and tuning considerations at inference time. Sequential Neural Likelihood (SNL) iteratively refines the surrogate likelihood by selecting parameters from the current approximate posterior, requiring an inference step at each round (Papamakarios et al., 2019; Durkan et al., 2018). NLE is often more effective when the parameter space is high-dimensional, whereas NPE is typically preferable when the observation space is high-dimensional, since mapping high-dimensional inputs to low-dimensional outputs is generally easier (Cranmer et al., 2020).

Generalized SBI solvers. Several methods target the joint distribution $p(\theta, \mathbf{y})$ to enable multiple inference queries through conditioning. Jointly Amortized Neural Approximation of Complex Bayesian Models (JANA) trains a summary network, posterior estimator, and likelihood model simultaneously, requiring careful balancing of multiple training objectives across networks (Radev et al., 2023). Similarly, Sequential Neural Posterior and Likelihood Approximation (SNPLA) learns both posterior and likelihood models using normalizing flows sequentially, but maintains separate estimators without a unified mechanism for arbitrary conditionals (Wiqvist et al., 2021). In contrast, Simformer trains a single Transformer-based score model on $p(\theta, \mathbf{y})$ and uses conditioning masks over tokenized variables to generate diverse conditionals from one set of parameters (Gloeckler et al., 2024). However, the Transformer-backbone brings complexity: self-attention scales quadratically with token count, reverse-time diffusion requires several iterative steps at inference, and the combination introduces a large hyperparameter space that can be challenging to tune. These limitations

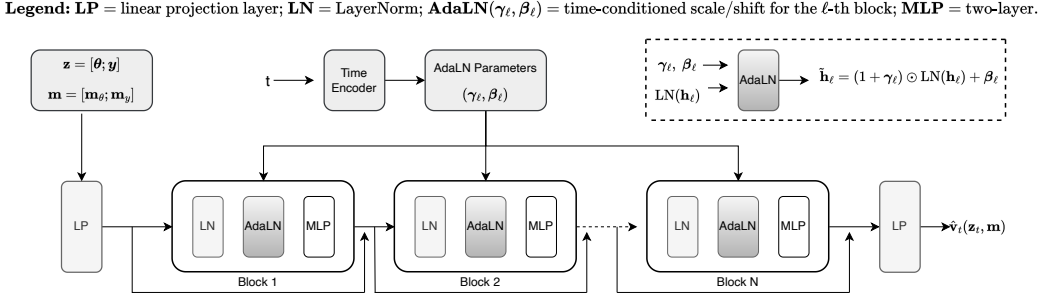


Figure 1. OneFlowSBI architecture. The flow network operates on the joint state $\mathbf{z}_t = (\boldsymbol{\theta}_t, \mathbf{y}_t)$, where observed and latent components are controlled by a binary mask \mathbf{m} . Conditioned on time t , the network learns a masked velocity field, yielding a single model of the joint distribution $p(\boldsymbol{\theta}, \mathbf{y})$.

become particularly pronounced in high-dimensional settings and when handling heterogeneous modalities such as images and spatiotemporal time series, where token counts, memory usage, and inference latency grow rapidly.

3. Preliminaries

Flow matching. Given data $\{\mathbf{x}_i\}_{i=1}^n$ with $\mathbf{x}_i \sim q(\mathbf{x})$, flow matching (Lipman et al., 2023) learns a generative model of $q(\mathbf{x})$ by constructing a continuous-time path of distributions $\{p_t\}_{t \in [0,1]}$ that connects a simple base distribution p_0 to the data distribution. Training minimizes the conditional flow matching (CFM) objective,

$$\mathcal{L}_{\text{CFM}}(\phi) = \mathbb{E}_{t, \mathbf{x}_1, \mathbf{x}_t} \left[\left\| \mathbf{v}_t^\phi(\mathbf{x}_t) - \mathbf{v}_t(\mathbf{x}_t \mid \mathbf{x}_1) \right\|_2^2 \right], \quad (1)$$

where $\mathbf{x}_1 \sim q(\mathbf{x})$, $\mathbf{x}_t \sim p_t(\mathbf{x}_t \mid \mathbf{x}_1)$, and \mathbf{v}_t^ϕ is a neural time-dependent vector field with parameters ϕ , while $\mathbf{v}_t(\mathbf{x}_t \mid \mathbf{x}_1)$ denotes the conditional target velocity. This conditional objective is tractable and equivalent to marginal flow matching since $p_t(\mathbf{x}_t) = \mathbb{E}_{\mathbf{x}_1 \sim q(\mathbf{x})} [p_t(\mathbf{x}_t \mid \mathbf{x}_1)]$. A common choice is optimal transport (OT), which couples $\mathbf{x}_0 \sim p_0$ with $\mathbf{x}_1 \sim q(\mathbf{x})$ via $\mathbf{x}_t = t \mathbf{x}_1 + (1 - t) \mathbf{x}_0$, yielding a constant conditional velocity $\mathbf{v}_t(\mathbf{x}_t \mid \mathbf{x}_1) = \mathbf{x}_1 - \mathbf{x}_0$. Sampling is performed by solving the ODE $\frac{d\mathbf{x}(t)}{dt} = \mathbf{v}_t^\phi(\mathbf{x}(t))$ forward from $t = 0$ to $t = 1$ with $\mathbf{x}_0 \sim p_0$, so that $\mathbf{x}_1 \sim q(\mathbf{x})$.

Masking and Conditional Generation. Mask-based conditioning provides a flexible mechanism for learning conditional distributions within a single generative model by explicitly encoding *missingness*. The paradigm originates from image inpainting, where binary masks distinguish observed pixels from missing regions, enabling models to perform completion under arbitrary masking patterns without task-specific retraining (Lugmayr et al., 2022). Related ideas appear in masked token prediction for transformer-based language and vision models (Devlin et al., 2019; He et al., 2022; Chang et al., 2022), where prediction targets are defined by arbitrary masking configurations.

Flow matching naturally complements mask-based condi-

tioning through its flexibility in specifying reference distributions (Lipman et al., 2023). Initializing generation from appropriately constructed reference distributions allows the induced flow to selectively evolve only the masked variables, while preserving observed coordinates as fixed boundary conditions throughout generation. This enables a single flow-matching model to parameterize a broad family of conditional distributions, with different conditioning patterns instantiated simply by varying the mask at generation time, without requiring separate models or retraining.

Motivated by these properties, we combine flow matching with mask-based conditioning to construct a unified framework for SBI. A single model is trained to represent the joint distribution $p(\boldsymbol{\theta}, \mathbf{y})$, from which arbitrary conditional distributions are realized through selective masking at inference time. The formal construction and training objective are presented in the next section.

4. Method

We model the joint distribution $p(\boldsymbol{\theta}, \mathbf{y})$ using a single flow-matching generative model, where $\boldsymbol{\theta} \in \mathbb{R}^{d_\theta}$ and $\mathbf{y} \in \mathbb{R}^{d_y}$ denote simulator parameters and observations of dimensions d_θ and d_y , respectively. Let $\mathbf{z} = [\boldsymbol{\theta}; \mathbf{y}] \in \mathbb{R}^{d_\theta + d_y}$ denote the joint latent variable, which defines the state space evolved by the flow. We introduce a binary mask $\mathbf{m} \in \{0, 1\}^{d_\theta + d_y}$, where $m_i = 1$ denotes an observed coordinate that remains fixed throughout the flow, and $m_i = 0$ denotes an unobserved coordinate that is transported by the flow. The mask defines subspaces over which probability mass is transported, encouraging a joint vector field that remains consistent across diverse conditioning patterns.

Building on the flow-matching formulation introduced in Section 2, we consider the following masked linear interpolant satisfying the boundary conditions $\mathbf{z}_0 \sim p_0$, where p_0 is a standard normal distribution defined on the unobserved subspace, and $\mathbf{z}_1 \sim p(\boldsymbol{\theta})p(\mathbf{y} \mid \boldsymbol{\theta})$, which is defined

for $t \in [0, 1]$ as,

$$\mathbf{z}_t = \mathbf{m} \odot \mathbf{z}_1 + (\mathbf{1} - \mathbf{m}) \odot (t \mathbf{z}_1 + (1 - t) \mathbf{z}_0), \quad (2)$$

which induces a tractable conditional path $p_t(\mathbf{z}_t \mid \mathbf{z}_1, \mathbf{m})$. Under this construction, transport occurs only along the unobserved coordinates, yielding a constant conditional target velocity along each trajectory,

$$\mathbf{v}_t(\mathbf{z}_t \mid \mathbf{z}_1, \mathbf{m}) = (\mathbf{1} - \mathbf{m}) \odot (\mathbf{z}_1 - \mathbf{z}_0). \quad (3)$$

To train the model, we define a masked conditional flow-matching objective derived from the conditional flow-matching loss in Eq. (1). We learn a time-dependent neural vector field $\mathbf{v}_t^\phi(\mathbf{z}_t, \mathbf{m})$ by matching the target velocity only on the coordinates designated as unobserved by the mask. We define the masked residual $\mathbf{r}_t^\phi := \mathbf{m}^c \odot (\mathbf{v}_t^\phi(\mathbf{z}_t, \mathbf{m}) - \mathbf{v}_t(\mathbf{z}_t \mid \mathbf{z}_1, \mathbf{m}))$, where $\mathbf{m}^c = \mathbf{1} - \mathbf{m}$ selects the unknown coordinates. The resulting *OneFlowSBI* loss is,

$$\mathcal{L}_{\text{OneFlowSBI}}(\phi) = \mathbb{E}_{t, \mathbf{z}_1, \mathbf{z}_t, \mathbf{m}} \left[\frac{1}{|\mathbf{m}^c|} \left\| \mathbf{w}^{1/2} \odot \mathbf{r}_t^\phi \right\|_2^2 \right], \quad (4)$$

where $|\mathbf{m}^c| = \sum_i m_i^c$ normalizes for different numbers of generated coordinates. In SBI, observations often have much higher dimensionality than parameters ($d_y \gg d_\theta$), causing the loss to be dominated by the observation block. To balance this, we set $w_i = \lambda_\theta$ for parameter dimensions ($i \leq d_\theta$) and $w_i = 1$ for observation dimensions ($i > d_\theta$), with $\lambda_\theta = d_y/d_\theta$ to equalize gradient magnitudes across the joint space. This masking mechanism ensures the joint vector field remains consistent across diverse conditioning patterns, enabling inference under arbitrary combinations of observed and unobserved variables.

Masking Approach. To optimize training for core SBI tasks, we define a masking distribution $p(\mathbf{m})$ as a mixture of primary inference modes,

$$p(\mathbf{m}) = \alpha \delta_{\mathbf{m}_{\text{post}}} + \beta \delta_{\mathbf{m}_{\text{like}}} + (1 - \alpha - \beta) p_{\text{partial}}(\mathbf{m}), \quad (5)$$

where weights $\alpha, \beta \geq 0$ satisfy $\alpha + \beta \leq 1$. Here, $\delta_{\mathbf{m}}$ denotes a Dirac point mass concentrated at \mathbf{m} , with $\mathbf{m}_{\text{post}} = [\mathbf{1}_{d_\theta}; \mathbf{0}_{d_y}]$ and $\mathbf{m}_{\text{like}} = [\mathbf{0}_{d_\theta}; \mathbf{1}_{d_y}]$ targeting full posterior and likelihood inference, respectively. The component p_{partial} facilitates broader generalization via a hierarchical sampling scheme: we draw hyperparameters $\pi_\theta, \pi_y \sim \text{Beta}(0.5, 0.5)$ and sample mask bits independently as $m_i \sim \text{Bernoulli}(\pi_\theta)$ for $i \leq d_\theta$ and $m_j \sim \text{Bernoulli}(\pi_y)$ for $j > d_\theta$. We set $\alpha = \beta = 0.15$, allocating 30% of training probability mass to the two core SBI queries, while the remaining 70% is assigned to partial conditioning. These weights lightly bias training toward the primary inference targets (posterior and likelihood) and can be adjusted to emphasize specific tasks as needed.

Inference via masking. Inference is carried out by integrating a mask-constrained ODE on the joint state space. For a

fixed mask \mathbf{m} , we initialize $\mathbf{z}_0 = \mathbf{m} \odot \mathbf{z}_{\text{obs}} + (\mathbf{1} - \mathbf{m}) \odot \boldsymbol{\varepsilon}$ with $\boldsymbol{\varepsilon} \sim \mathcal{N}(\mathbf{0}, \mathbf{I})$, and evolve the trajectory \mathbf{z}_t as,

$$\frac{d\mathbf{z}_t}{dt} = (\mathbf{1} - \mathbf{m}) \odot \mathbf{v}_t^\phi(\mathbf{z}_t, \mathbf{m}), \quad (6)$$

for $t \in [0, 1]$. These dynamics leave the masked coordinates invariant, i.e. $\mathbf{m} \odot \mathbf{z}_t = \mathbf{m} \odot \mathbf{z}_{\text{obs}}$ for all t , while transporting probability mass only along the complementary subspace. The terminal state \mathbf{z}_1 therefore constitutes a sample from the conditional distribution specified by the mask.

Standard SBI tasks are recovered as special cases of the joint model by applying specific mask configurations (Table 1). By clamping observed variables and integrating the vector field over the remaining coordinates, a single model can transition between posterior sampling, likelihood evaluation, and joint modeling. This framework naturally handles missing data by leaving the corresponding dimensions unmasked. More generally, the model supports arbitrary mixed conditionals $p(\mathbf{z}_A \mid \mathbf{z}_B)$ for any disjoint subsets A and B , enabling flexible inference across diverse observation patterns without task-specific architectures or retraining.

Table 1. Mask specifications for SBI. Block masks use $\mathbf{0}$ for generated variables, $\mathbf{1}$ for conditioned variables, and \times for ignored variables. For mixed conditionals, the full variable vector \mathbf{z} is partitioned into disjoint subsets A (generated) and B (conditioned), with dimensions $d_A = |A|$ and $d_B = |B|$.

Task	Target density	Mask \mathbf{m}
Posterior	$p(\theta \mid \mathbf{y}_{\text{obs}})$	$[\mathbf{0}_{d_\theta}; \mathbf{1}_{d_y}]$
Likelihood	$p(\mathbf{y} \mid \theta_{\text{obs}})$	$[\mathbf{1}_{d_\theta}; \mathbf{0}_{d_y}]$
Joint	$p(\theta, \mathbf{y})$	$[\mathbf{0}_{d_\theta}; \mathbf{0}_{d_y}]$
Prior	$p(\theta)$	$[\mathbf{0}_{d_\theta}; \times]$
Marginal	$p(\mathbf{y})$	$[\times; \mathbf{0}_{d_y}]$
Mixed conditional	$p(\mathbf{z}_A \mid \mathbf{z}_B)$	$[\mathbf{0}_{d_A}; \mathbf{1}_{d_B}]$

Computational complexity. Training requires a single evaluation of the vector field $\mathbf{v}_t^\phi(\mathbf{z}_t, \mathbf{m})$ per sampled tuple $(\mathbf{z}_1, \mathbf{z}_0, t, \mathbf{m})$, as the objective in Eq. (4) consists of a single regression target along the masked probability path. At inference, generating one sample amounts to integrating a deterministic ODE with K discretization steps, resulting in $O(K)$ evaluations of \mathbf{v}_t^ϕ per sample. This cost is independent of the conditioning pattern - the mask only restricts which coordinates are updated through element-wise gating, while the vector field is evaluated once per step on the full joint state. Owing to the masked linear interpolant and the resulting smooth, near-linear transport geometry, accurate sampling is typically achieved with a small number of integration steps (Liu et al., 2023).

Model architecture. The *OneFlowSBI* model architecture is shown in Figure 1. We parameterize the masked vector field $\mathbf{v}_t^\phi(\mathbf{z}_t, \mathbf{m})$ using a lightweight residual MLP with Adaptive LayerNorm (AdaLN) blocks (Peebles & Xie, 2023). The joint state \mathbf{z}_t and mask \mathbf{m} are mapped to a

hidden representation via a linear projection, while time t is encoded using a sinusoidal embedding (Vaswani et al., 2017) and transformed into AdaLN scale and shift parameters (γ_ℓ, β_ℓ). The backbone consists of L residual blocks indexed by ℓ , each applying LayerNorm, AdaLN modulation, and a two-layer MLP,

$$\mathbf{h}_{\ell+1} = \mathbf{h}_\ell + \text{MLP}_\ell \left((1 + \gamma_\ell) \odot \text{LN}(\mathbf{h}_\ell) + \beta_\ell \right). \quad (7)$$

A final linear projection outputs the velocity in $\mathbb{R}^{d_\theta + d_y}$. We zero-initialize the AdaLN parameter heads and the output projection so that $\mathbf{v}_t^\phi(\mathbf{z}_t, \mathbf{m}) \approx \mathbf{0}$ at initialization, improving training stability.

5. Experiments

We evaluate *OneFlowSBI* on the Simulation-Based Inference Benchmark (SBIBM) (Lueckmann et al., 2021), comprising 10 tasks covering diverse inference regimes including multimodal posteriors, strong parameter-observation dependencies, noisy observations, and moderately high-dimensional spaces. We also consider two high-dimensional real-world problems: Bayesian image deblurring with implicit priors over Fashion-MNIST ($\theta, \mathbf{y} \in \mathbb{R}^{784}$) (Radev et al., 2023), and the shallow water model, which infers basin depth profiles ($\theta \in \mathbb{R}^{100}$) from spatiotemporal wave fields ($\mathbf{y} \in \mathbb{R}^{20,200}$) (Ramesh et al., 2022). These tasks evaluate scalability across heterogeneous modalities, from image-based to time-dependent physical field inference.

5.1. Experimental setup

To study how performance scales with simulation budget (often the primary bottleneck when simulator calls are expensive), we train models with 10,000, 20,000, and 30,000 simulated pairs, reporting results over 5 independent runs for each SBIBM task and budget. At evaluation, we approximate posteriors for 10 held-out test observations by drawing 10,000 samples under the posterior mask, conditioning on the observation block while generating the parameter block. Posterior accuracy is measured using the classifier two-sample test (C2ST; Friedman, 2003), comparing learned posterior samples against SBIBM reference posteriors obtained analytically or via high-fidelity numerical approximations such as long-run MCMC (Lueckmann et al., 2021). C2ST accuracy varies within $[0.5, 1]$, with endpoints 0.5 (perfect match) and 1 (complete mismatch).

We compare *OneFlowSBI* against Simformer (Gloeckler et al., 2024) in two configurations, a black-box dense setting with full interactions between all components of the parameters and data, and a structured undirected setting with mask-restricted interactions reflecting known simulator structure, alongside NPE, a widely used specialized posterior estimator that serves as a standard SBI baseline (Papa-

makarios & Murray, 2016). We also report maximum mean discrepancy (MMD) as a complementary metric in the supplementary material, with hyperparameters in Appendix C and full results tables and additional analyses (including posterior plots) in Appendices D and E.

5.2. Benchmark results

Figure 2 summarizes C2ST performance across ten SBIBM benchmarks under three simulation budgets, comparing *OneFlowSBI* against NPE, Simformer-Dense (Simformer-D), and Simformer-Undirected (Simformer-U). To analyze these results, we categorize the benchmarks into three regimes based on dimensionality and structural complexity:

Low-Dimensional and Structured Tasks. In low-dimensional regimes such as Two Moons and the Gaussian Mixture Model (GMM), *OneFlowSBI* achieves near-optimal C2ST scores (approximately 0.5), indicating high posterior fidelity. Performance is comparable to both Simformer variants across these benchmarks, while substantially outperforming NPE. On the Gaussian Linear task, *OneFlowSBI* matches the performance of Simformer-U while outperforming NPE and Simformer-D. In the non-conjugate Gaussian Linear Uniform setting, Simformer-U leverages its structured masking to achieve the highest accuracy, though *OneFlowSBI* remains competitive and consistently surpasses NPE.

High-Dimensionality and Distractors. Comparing Simple Likelihood Complex Posterior (SLCP) with its Distractors variant (with 92 noise dimensions) reveals critical trade-off in architectural inductive biases. Simformer-U excels on vanilla SLCP by exploiting known i.i.d. observation structure through its mask, but degrades sharply on Distractors where restricted masking prevents the interactions needed to separate signal from high-dimensional noise. Conversely, Simformer-D leverages unrestricted global attention to effectively filter distractors. Notably, *OneFlowSBI* remains robust and outperforms the NPE baseline across both datasets. This result is achieved despite learning the full joint distribution without attention mechanisms which requires dedicating substantial capacity to irrelevant distractor structure yet still allows accurate recovery of the complex multi modal posterior geometry.

Biological and Ecological Models. *OneFlowSBI* achieves the lowest C2ST scores on the Bernoulli Generalized Linear Model (GLM) and its high-dimensional variant (GLM-Raw) at the largest simulation budgets. Similar accuracy gains are observed on the Susceptible-Infected-Recovered (SIR) model. For Lotka-Volterra, all methods yield C2ST values near 1.0. This is a consequence of the extremely concentrated reference posterior (per-dimension variance $\approx 10^{-4}$), which leads to C2ST saturation and limits the metric's discriminative utility in this specific regime.

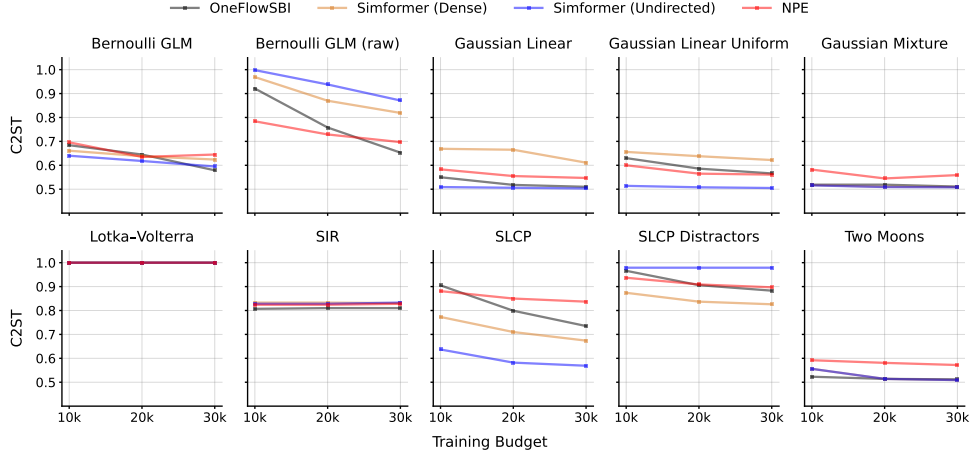


Figure 2. SBIBM benchmark results. C2ST across ten benchmark tasks and three simulation budgets (10,000; 20,000; 30,000), comparing *OneFlowSBI* with Simformer (Dense), Simformer (Undirected), and NPE. Lower C2ST indicates higher posterior fidelity.

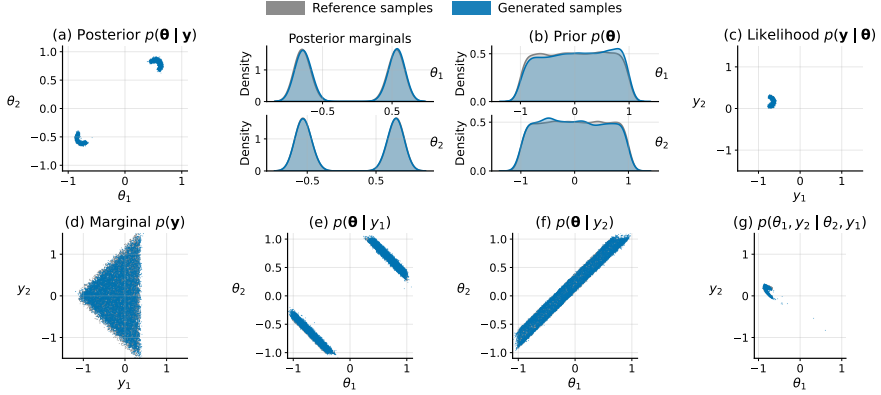


Figure 3. Multi-query inference on Two Moons. Using a single *OneFlowSBI* model, we target diverse densities $p(\cdot|\cdot)$ solely by varying the inference mask. Panels show the (a) posterior, (b) prior, (c) likelihood, and (d) evidence, alongside (e–g) arbitrary partial conditionals.

Unified multi-target inference. To demonstrate multi-query inference with a single trained model, we present qualitative results on the Two Moons task in Figure 3. We obtain different inference queries by modifying only the conditioning mask, generating 10,000 samples for seven settings: (a) posterior inference $p(\theta | y)$, (b) prior recovery $p(\theta)$, (c) likelihood sampling $p(y | \theta)$, (d) the data marginal $p(y)$, (e,f) partial conditionals $p(\theta | y_1)$ and $p(\theta | y_2)$, and (g) a mixed conditional $p(\theta_1, y_2 | \theta_2, y_1)$. Reference samples for posteriors are provided by SBIBM, while likelihoods and marginals follow the benchmark specification. For partial and mixed conditionals, references are generated using hybrid Slice sampling and Gaussian Metropolis-Hastings (Gloeckler et al., 2024). *OneFlowSBI* accurately matches reference distributions across all queries, faithfully recovering the bimodal observation structure, multimodal posterior geometry, uniform prior, and lower-dimensional manifolds under partial conditioning. Notably, the partial and mixed conditionals in (e,f,g) demonstrate coherent

dependencies that would each require training a separate model in traditional SBI approaches. This flexibility to query arbitrary conditionals through masking alone makes *OneFlowSBI* valuable for exploratory workflows where the inference task may not be fully specified in advance.

5.3. Real World Problems

Bayesian image deblurring. This test problem involves 784-dimensional noisy, blurred observations from Fashion-MNIST, with the goal being inference of the corresponding clean image (Ramesh et al., 2022; Radev et al., 2023). This task is challenging as blurring destroys fine-scale spatial information while noise introduces further ambiguity, yielding a multimodal posterior where multiple distinct images can plausibly explain the same observation. Additionally, this experiment tests how *OneFlowSBI* scales to image-modality inference, where strong spatial structure and local correlations differ fundamentally from the vector-valued, low-dimensional SBIBM tasks (Additional details on the

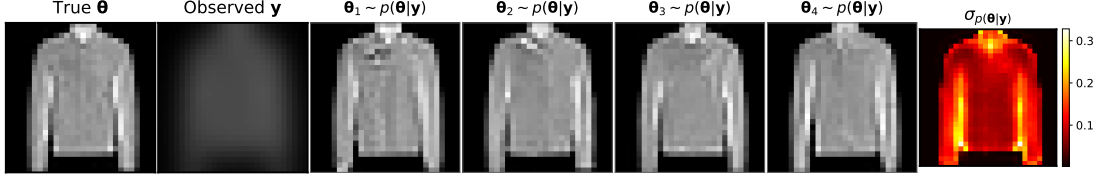


Figure 4. Posterior inference for Bayesian image deblurring. We visualize the ability of *OneFlowSBI* to recover the posterior $p(\theta | y)$ from a noisy, blurred observation y . The posterior samples $\hat{\theta}_{1:4}$ demonstrate high-frequency detail recovery, while the uncertainty map σ (right) effectively captures the combined effects of pixel-level noise and information loss due to the blur kernel, particularly at object boundaries.

simulation settings are provided in Appendix B.3.)

We train *OneFlowSBI* with a simulation budget of 30,000 samples, and generate 1000 posterior samples for a fixed parameter-observation pair. Figure 4 visualizes posterior predictions for an example observation depicting a shirt, showing the first four samples along with the posterior standard deviation over the full sample set. The samples remain visually consistent with the underlying garment while differing in fine-scale details, indicating meaningful posterior uncertainty. Reconstructions preserve the dominant structure, with most variation concentrated in regions where blur and noise remove high-frequency information. The posterior standard deviation map exhibits clear spatial structure, with elevated uncertainty along edges and other high-frequency regions most affected by degradation, demonstrating that the model captures uncertainty rather than collapsing to a deterministic point estimate. Training procedures and hyperparameters, along with baseline comparisons and additional results are provided in Appendix D.2.

Shallow water inverse problem. Here we infer a 100-dimensional parameter vector from surface-wave observations generated by numerically solving the 1-D Saint-Venant equations (Ramesh et al., 2022). Observations are Fourier-domain wavefields with real and imaginary components over time and space, forming tensors of shape $2 \times 101 \times 100$. This inverse problem is challenging because the observation space is much larger and structurally different than the parameter space. Also, local parameter perturbations induce nonlinear propagation effects that influence the wavefield globally, yielding complex and highly nonlocal parameter-observation dependencies. Further setup details are provided in Appendix B.3.

We train *OneFlowSBI* using 30,000 simulations; implementation details and hyperparameters are listed in Appendix C.3. As ground-truth posteriors are unavailable, we fix a parameter-observation pair for evaluation, drawing 100 posterior samples, and report posterior predictive checks in Figure 5. Panel (a) shows inferred depth-profile samples concentrating around the true depth, with increased uncertainty in regions where the wave observations are less informative. Panels (b-d) compare observed and predicted wave

amplitudes at selected time steps, showing close agreement in both phase and amplitude across space. Full spatiotemporal wavefields in panels (e-f) further confirm that posterior predictive samples capture the global propagation dynamics over the entire observation window. See Appendix D.3 for additional results, including NPE baselines.

6. Ablations

In this ablation, we probe the practical deployment properties of *OneFlowSBI*: a single reusable inference model that supports diverse query types across modalities and remains robust under noisy or corrupted observations. We evaluate robustness under additive observation noise and partial observability, and analyze sampling efficiency by varying the number of ODE solver steps used at inference.

Quantitative robustness to observation noise. Real measurements are often noisy due to sensor constraints and the acquisition pipeline, motivating an assessment of inference methods in the presence of observation noise. We evaluate posterior inference under additive Gaussian noise, $\tilde{y}_{\text{obs}} = y_{\text{obs}} + \mathcal{N}(0, \sigma^2 I)$, for the Gaussian Linear, Gaussian Linear Uniform, Bernoulli GLM, and Bernoulli GLM (raw) tasks, using models trained on 30,000 simulations. We vary the noise level σ over the range $\{0, 0.1, 0.25, 0.5, 0.75, 1\}$. Figure 6(a) shows monotonic C2ST increase with σ , reflecting the expected degradation as signal-to-noise ratio decreases. The degradation pattern is strongly task-dependent: the Bernoulli GLM exhibits high sensitivity, while the Gaussian Linear task remains robust under moderate noise, with Gaussian Linear Uniform and Bernoulli GLM (raw) showing intermediate behavior. Importantly, performance remains acceptable for practical noise levels ($\sigma \leq 0.5$) across most tasks, with severe degradation only occurring at high noise levels ($\sigma \geq 0.75$) where observations become insufficiently informative. This ablation demonstrates that *OneFlowSBI* maintains reliable posterior inference under realistic measurement noise and degrades predictably only when noise severely dominates the signal.

Quantitative robustness to missing observations. In real-world experiments, observations are often incomplete due

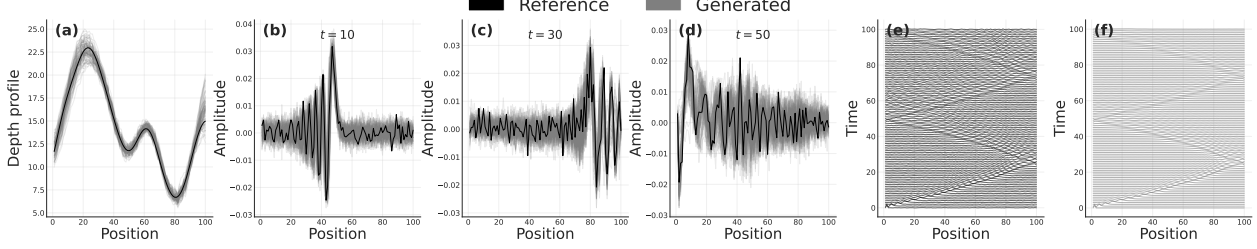


Figure 5. Posterior predictive checks for shallow water inference. (a) Posterior samples of the inferred depth profile compared to the ground truth. (b–d) Wave amplitudes at selected time steps comparing observed and posterior predictive wavefields. (e–f) Full spatiotemporal wavefields illustrating posterior predictive reconstructions over time.

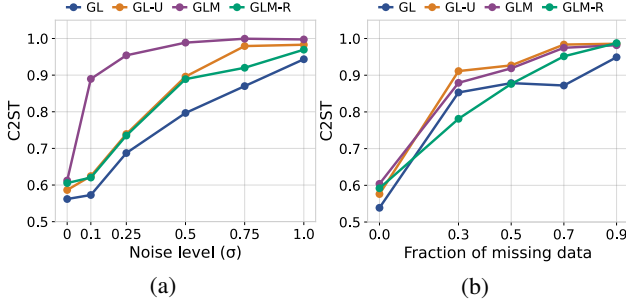


Figure 6. OneFlowSBI robustness. (a) Posterior robustness to additive observation noise. (b) Posterior robustness to missing observations. Both evaluated using C2ST.

to sensor failures, occlusions, selective acquisition, or corruption, motivating an evaluation of robustness under partial observability. Using the setup as above, we perform posterior inference when only a subset of observation coordinates are available. At test time, we randomly mask a fraction $\rho \in \{0.0, 0.3, 0.5, 0.7, 0.9\}$ of the observation dimensions (missingness rate) and sample $p(\theta | \mathbf{y}_{\text{obs}})$ using the posterior mask. For each ρ , we draw 10,000 samples and compute C2ST against reference posteriors. Figure 6(b) shows monotonic C2ST increase with ρ , reflecting progressive information loss. Performance remains stable for low/moderate missingness ($\rho \leq 0.5$) across tasks, demonstrating effective handling of partial observations. Sharp degradation occurs only at high missingness levels ($\rho \geq 0.7$), where C2ST approaches 1 as expected when observations become insufficiently informative for posterior identification. This ablation confirms that *OneFlowSBI* robustly handles realistic missing data scenarios, with performance degrading only when the majority of observations are unavailable.

Sampling efficiency. Since *OneFlowSBI* targets repeated and diverse inference queries with a single model, fast sampling is essential for practical deployment. We study how ODE discretization steps affect posterior accuracy on two high-dimensional problems (Shallow Water and Bayesian Denoising). For each task, we draw 100 posterior samples using an Euler solver and compute the MSE between the posterior mean and ground truth for step counts from 1 to

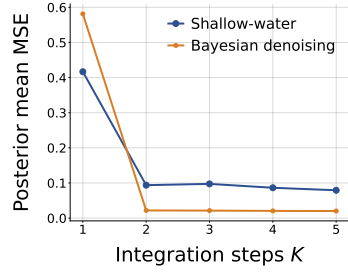


Figure 7. Mean squared error (MSE) of the posterior mean with respect to the ground-truth as a function of the number of ODE discretization steps at inference.

5. Figure 7 shows that only 2–3 steps are sufficient for near-optimal performance: error drops sharply in this range and saturates thereafter with no systematic gains beyond 3 steps. This sampling efficiency stems from the geometry induced by flow matching with masked linear interpolants. The conditional velocity field in Eq. (2) is directionally constant on unobserved coordinates and varies smoothly only in magnitude, yielding near-straight transport paths between the noise distribution and the posterior. Consequently, accurate ODE integration succeeds even under coarse discretization. In contrast, score-based diffusion methods like Simformer require iterative stochastic denoising over many steps to follow curved drift–diffusion trajectories, incurring substantially higher per-query cost (Gloeckler et al., 2024). This efficiency makes *OneFlowSBI* well-suited for rapid multi-query inference.

7. Conclusion

We presented *OneFlowSBI*, a unified framework for simulation-based inference that approximates the joint distribution of parameters and observations through a single flow matching model. Combining dynamic coordinate masking with a stable regression objective, the method supports a full spectrum of inference queries - from standard posterior estimation to likelihood surrogates, without the need for task-specific retraining. Empirical evaluations demonstrate that *OneFlowSBI* outperforms or matches state-of-the-art

specialized and generalized solvers across a majority of benchmarks, while exhibiting robustness to partial or noisy data. Further, exploiting the straight-line geometry of optimal transport, the framework ensures efficient deterministic sampling independent of the underlying neural architecture. *OneFlowSBI* thus offers a flexible framework for amortized SBI supporting unified multi-query inference with minimal overhead across dimensionalities and modalities.

Impact Statement

This paper introduces a unified simulation based inference method that supports multiple inference queries across scientific and engineering applications. As with any SBI approach, validity depends on the simulator and prior: misspecification can lead to biased posteriors and overconfident conclusions. In deployment, users should check modeling assumptions, perform posterior predictive diagnostics, and interpret uncertainty in line with domain knowledge and measurement noise. We do not anticipate broader societal impacts beyond the general risks associated with probabilistic machine learning models.

References

Akiba, T., Sano, S., Yanase, T., Ohta, T., and Koyama, M. Optuna: A next-generation hyperparameter optimization framework. In *The 25th ACM SIGKDD International Conference on Knowledge Discovery & Data Mining*, pp. 2623–2631, 2019.

Beaumont, M. A., Zhang, W., and Balding, D. J. Approximate bayesian computation in population genetics. *Genetics*, 162(4):2025–2035, Dec 2002. doi: 10.1093/genetics/162.4.2025.

Chang, H., Zhang, H., Jiang, L., Liu, C., and Freeman, W. T. Maskgit: Masked generative image transformer. In *2022 IEEE/CVF Conference on Computer Vision and Pattern Recognition (CVPR)*, pp. 11305–11315, 2022. doi: 10.1109/CVPR52688.2022.01103.

Chen, R. T. Q. torchdiffeq, 2018. URL <https://github.com/rtqichen/torchdiffeq>.

Cranmer, K., Brehmer, J., and Louppe, G. The frontier of simulation-based inference. *Proceedings of the National Academy of Sciences*, 117(48):30055–30062, 2020.

Devlin, J., Chang, M.-W., Lee, K., and Toutanova, K. Bert: Pre-training of deep bidirectional transformers for language understanding. In *North American Chapter of the Association for Computational Linguistics*, 2019.

Durkan, C., Papamakarios, G., and Murray, I. Sequential neural methods for likelihood-free inference. *ArXiv*, abs/1811.08723, 2018.

Friedman, J. H. On multivariate goodness-of-fit and two-sample testing. *Statistical Problems in Particle Physics, Astrophysics, and Cosmology*, 1:311, 2003.

Geffner, T., Papamakarios, G., and Mnih, A. Compositional score modeling for simulation-based inference. In *International Conference on Machine Learning*, pp. 11098–11116. PMLR, 2023.

Gloeckler, M., Deistler, M., Weilbach, C., Wood, F., and Macke, J. H. All-in-one simulation-based inference. In *Proceedings of the 41st International Conference on Machine Learning*, ICML’24. JMLR.org, 2024.

Greenberg, D., Nonnenmacher, M., and Macke, J. Automatic posterior transformation for likelihood-free inference. In *International Conference on Machine Learning*, pp. 2404–2414. PMLR, 2019.

He, K., Chen, X., Xie, S., Li, Y., Dollár, P., and Girshick, R. Masked autoencoders are scalable vision learners. In *2022 IEEE/CVF Conference on Computer Vision and Pattern Recognition (CVPR)*, pp. 15979–15988, 2022. doi: 10.1109/CVPR52688.2022.01553.

Kingma, D. and Ba, J. Adam: A method for stochastic optimization. *International Conference on Learning Representations*, 12 2014.

Lavin, A., Zenil, H., Paige, B., Krakauer, D. C., Gottschlich, J. E., Mattson, T. G., Anandkumar, A., Choudry, S., Rocki, K., Baydin, A. G., Prunkl, C. E. A., Isayev, O., Peterson, E. J., McMahon, P. L., Macke, J. H., Cranmer, K., Zhang, J., Wainwright, H. M., Hanuka, A., Veloso, M. M., Assefa, S. A., Zheng, S., and Pfeffer, A. Simulation intelligence: Towards a new generation of scientific methods. *ArXiv*, abs/2112.03235, 2021.

Lee, S., Lin, Z., and Fanti, G. Improving the training of rectified flows. In *The Thirty-eighth Annual Conference on Neural Information Processing Systems*, 2024.

Lipman, Y., Chen, R. T. Q., Ben-Hamu, H., Nickel, M., and Le, M. Flow matching for generative modeling. In *The Eleventh International Conference on Learning Representations*, 2023.

Liu, X., Gong, C., and Liu, Q. Flow straight and fast: Learning to generate and transfer data with rectified flow. *The Eleventh International Conference on Learning Representations*, 2023.

Lueckmann, J.-M., Goncalves, P. J., Bassetto, G., Öcal, K., Nonnenmacher, M., and Macke, J. H. Flexible statistical inference for mechanistic models of neural dynamics. In *Advances in Neural Information Processing Systems*, volume 30. Curran Associates, Inc., 2017.

Lueckmann, J.-M., Boelts, J., Greenberg, D., Goncalves, P., and Macke, J. Benchmarking simulation-based inference. In *Proceedings of The 24th International Conference on Artificial Intelligence and Statistics*, volume 130 of *Proceedings of Machine Learning Research*, pp. 343–351. PMLR, 13–15 Apr 2021.

Lugmayr, A., Danelljan, M., Romero, A., Yu, F., Timofte, R., and Van Gool, L. Repaint: Inpainting using denoising diffusion probabilistic models. In *2022 IEEE/CVF Conference on Computer Vision and Pattern Recognition (CVPR)*, pp. 11451–11461, 2022. doi: 10.1109/CVPR52688.2022.01117.

Papamakarios, G. and Murray, I. Fast ε -free inference of simulation models with bayesian conditional density estimation. *Advances in neural information processing systems*, 29, 2016.

Papamakarios, G., Sterratt, D., and Murray, I. Sequential neural likelihood: Fast likelihood-free inference with autoregressive flows. In Chaudhuri, K. and Sugiyama, M. (eds.), *Proceedings of the Twenty-Second International Conference on Artificial Intelligence and Statistics*, volume 89 of *Proceedings of Machine Learning Research*, pp. 837–848. PMLR, 16–18 Apr 2019.

Peebles, W. and Xie, S. Scalable diffusion models with transformers. In *Proceedings of the IEEE/CVF International Conference on Computer Vision (ICCV)*, pp. 4195–4205, October 2023.

Radev, S. T., Schmitt, M., Pratz, V., Picchini, U., Köthe, U., and Bürkner, P.-C. Jana: Jointly amortized neural approximation of complex bayesian models. In *Uncertainty in Artificial Intelligence*, pp. 1695–1706. PMLR, 2023.

Ramesh, P., Lueckmann, J.-M., Boelts, J., Tejero-Cantero, Á., Greenberg, D. S., Goncalves, P. J., and Macke, J. H. GATSBI: Generative adversarial training for simulation-based inference. In *International Conference on Learning Representations*, 2022.

Sisson, S. A., Fan, Y., and Beaumont, M. *Handbook of approximate Bayesian computation*. CRC press, 2018.

Toni, T., Welch, D., Strelkowa, N., Ipsen, A., and Stumpf, M. P. Approximate bayesian computation scheme for parameter inference and model selection in dynamical systems. *Journal of the Royal Society Interface*, 6(31): 187–202, 2009. doi: 10.1098/rsif.2008.0172.

Vaswani, A., Shazeer, N., Parmar, N., Uszkoreit, J., Jones, L., Gomez, A. N., Kaiser, L. u., and Polosukhin, I. Attention is all you need. In Guyon, I., Luxburg, U. V., Bengio, S., Wallach, H., Fergus, R., Vishwanathan, S., and Garnett, R. (eds.), *Advances in Neural Information Processing Systems*, volume 30. Curran Associates, Inc., 2017.

Villani, C. *Optimal Transport: Old and New*, volume 338 of *Grundlehren der mathematischen Wissenschaften*. Springer, 2009.

Wildberger, J., Dax, M., Buchholz, S., Green, S., Macke, J. H., and Schölkopf, B. Flow matching for scalable simulation-based inference. In Oh, A., Naumann, T., Globerson, A., Saenko, K., Hardt, M., and Levine, S. (eds.), *Advances in Neural Information Processing Systems*, volume 36, pp. 16837–16864. Curran Associates, Inc., 2023.

Wiqvist, S., Frellsen, J., and Picchini, U. Sequential neural posterior and likelihood approximation, 2021.

A. Conditional Probability-Flow Validity Under Masking

OneFlowSBI implements conditioning by treating a masked subset of coordinates as observed (fixed) while learning a probability flow over the remaining unobserved coordinates. This section formalizes why these masked dynamics yield a valid, mass-conserving probability flow that is consistent with the time-evolving conditional density.

Let $\mathbf{z} = (\boldsymbol{\theta}, \mathbf{y}) \in \mathbb{R}^d$ denote the joint vector of parameters and observations with density $p(\mathbf{z})$. A binary mask partitions \mathbf{z} into two disjoint components,

$$\mathbf{z} = (\mathbf{z}_A, \mathbf{z}_B) \in \mathbb{R}^{d_A} \times \mathbb{R}^{d_B}, \quad d = d_A + d_B, \quad (8)$$

where \mathbf{z}_A denotes the unobserved coordinates to be generated and \mathbf{z}_B denotes the observed coordinates used for conditioning.

At $t = 0$, we initialize the unobserved block by sampling $\mathbf{z}_A \sim p_0(\mathbf{z}_A)$ from a tractable reference distribution, while fixing \mathbf{z}_B to observed values drawn from the data marginal $p(\mathbf{z}_B)$. The initialization thus factorizes as $p_0(\mathbf{z}_A, \mathbf{z}_B) = p_0(\mathbf{z}_A)p(\mathbf{z}_B)$, under the assumption that the initial noise \mathbf{z}_A is sampled independently of the observed constraints \mathbf{z}_B before the generative process introduces their coupling.

We define a time-indexed conditional probability path,

$$p_t(\mathbf{z}_A, \mathbf{z}_B) = p_t(\mathbf{z}_A \mid \mathbf{z}_B)p(\mathbf{z}_B), \quad t \in [0, 1], \quad (9)$$

with boundary conditions $p_0(\mathbf{z}_A \mid \mathbf{z}_B) = p_0(\mathbf{z}_A)$ and $p_1(\mathbf{z}_A \mid \mathbf{z}_B) = p(\mathbf{z}_A \mid \mathbf{z}_B)$.

The masked vector field evolves only the unobserved coordinates while keeping the observed coordinates fixed,

$$\frac{d}{dt} \mathbf{z}_t = \mathbf{v}_t(\mathbf{z}_t), \quad \mathbf{z}_t = (\mathbf{z}_{t,A}, \mathbf{z}_{t,B}), \quad \mathbf{v}_t(\mathbf{z}_A, \mathbf{z}_B) = \begin{pmatrix} \mathbf{v}_{t,A}(\mathbf{z}_A, \mathbf{z}_B) \\ \mathbf{0}_{d_B} \end{pmatrix}, \quad (10)$$

where $\mathbf{0}_{d_B} \in \mathbb{R}^{d_B}$ denotes the zero vector.

Theorem A.1 (Conditional continuity equation). *Suppose the joint density $p_t(\mathbf{z}_A, \mathbf{z}_B)$ evolves under the masked vector field (10) and satisfies the joint continuity equation (Villani, 2009),*

$$\frac{\partial p_t(\mathbf{z}_A, \mathbf{z}_B)}{\partial t} + \nabla_{\mathbf{z}} \cdot (p_t(\mathbf{z}_A, \mathbf{z}_B) \mathbf{v}_t(\mathbf{z}_A, \mathbf{z}_B)) = 0, \quad (11)$$

then for any fixed \mathbf{z}_B in the support of $p(\mathbf{z}_B)$, the conditional density $p_t(\mathbf{z}_A \mid \mathbf{z}_B)$ satisfies,

$$\frac{\partial p_t(\mathbf{z}_A \mid \mathbf{z}_B)}{\partial t} + \nabla_{\mathbf{z}_A} \cdot [p_t(\mathbf{z}_A \mid \mathbf{z}_B) \mathbf{v}_{t,A}(\mathbf{z}_A, \mathbf{z}_B)] = 0. \quad (12)$$

Proof. Expanding the divergence in (11) using $\mathbf{v}_{t,B} = \mathbf{0}$ yields,

$$\frac{\partial p_t(\mathbf{z}_A, \mathbf{z}_B)}{\partial t} + \nabla_{\mathbf{z}_A} \cdot (p_t(\mathbf{z}_A, \mathbf{z}_B) \mathbf{v}_{t,A}(\mathbf{z}_A, \mathbf{z}_B)) = 0. \quad (13)$$

Substituting the factorization (9) gives,

$$p(\mathbf{z}_B) \frac{\partial p_t(\mathbf{z}_A \mid \mathbf{z}_B)}{\partial t} + \nabla_{\mathbf{z}_A} \cdot (p_t(\mathbf{z}_A \mid \mathbf{z}_B) p(\mathbf{z}_B) \mathbf{v}_{t,A}(\mathbf{z}_A, \mathbf{z}_B)) = 0. \quad (14)$$

Since $p(\mathbf{z}_B)$ is constant with respect to \mathbf{z}_A and t , it factors out of the divergence,

$$p(\mathbf{z}_B) \left[\frac{\partial p_t(\mathbf{z}_A \mid \mathbf{z}_B)}{\partial t} + \nabla_{\mathbf{z}_A} \cdot (p_t(\mathbf{z}_A \mid \mathbf{z}_B) \mathbf{v}_{t,A}(\mathbf{z}_A, \mathbf{z}_B)) \right] = 0. \quad (15)$$

For \mathbf{z}_B in the support of $p(\mathbf{z}_B)$, we have $p(\mathbf{z}_B) > 0$, which implies (12). \square

This establishes that the masked ODE defines a *mass-conserving conditional flow*: for each fixed \mathbf{z}_B , the vector field $\mathbf{v}_{t,A}$ induces a valid probability evolution of $p_t(\mathbf{z}_A \mid \mathbf{z}_B)$. Consequently, one can train $\mathbf{v}_{t,A}$ via flow matching conditioned on \mathbf{z}_B , and integrating the masked ODE yields samples from $p(\mathbf{z}_A \mid \mathbf{z}_B)$ at $t = 1$ while keeping \mathbf{z}_B fixed.

B. Task Description

In this section, we describe the priors defining the parameter inference search space, and simulator settings used to generate the datasets for all benchmark problems reported in the main text.

B.1. SBIBM Tasks

The Simulation-Based Inference Benchmark (SBIBM) suite comprises ten canonical problems designed to evaluate inference methods across a range of posterior structures and simulator behaviors encountered in practice. The tasks span linear and nonlinear models, stochastic dynamics, and multimodal posteriors, including Gaussian linear models, SLCP variants, Bernoulli GLMs, Gaussian mixtures, two-moons, SIR, and the Lotka-Volterra predator-prey model. We adopt the standard priors, simulators, and protocols; full specifications are in [Lueckmann et al. \(2021\)](#) (supplementary Tasks T.1–T.10).

B.2. Shallow Water Problem

For this task, the goal is to infer an unknown basin depth profile, represented as a 100-dimensional vector drawn from a Gaussian prior,

$$p(\boldsymbol{\theta}) = \mathcal{N}(\mu \mathbf{1}_{100}, \boldsymbol{\Sigma}), \quad \Sigma_{ij} = \sigma^2 \exp\left(-\frac{(i-j)^2}{\tau}\right), \quad (16)$$

where $\mu = 10$, $\sigma = 15$, and $\tau = 100$. This squared-exponential kernel induces smooth depth profiles while retaining sufficient variability for identifiability: the chosen hyperparameters yield distinct simulator responses, whereas reduced variance or excessive smoothness lead to near-degenerate observations ([Ramesh et al., 2022](#)).

The simulation model is defined as,

$$\mathbf{y} = f(\boldsymbol{\theta}) + \sigma_\varepsilon \boldsymbol{\varepsilon}, \quad \boldsymbol{\varepsilon}_{ij} \sim \mathcal{N}(0, 1), \quad (17)$$

where $\sigma_\varepsilon = 0.25$ and $f(\boldsymbol{\theta}) \in \mathbb{R}^{2 \times 100 \times 100}$ is the stacked real and imaginary parts of the two-dimensional Fourier transform of the surface wave field. The wave field is obtained by solving the one-dimensional Saint-Venant equations on a spatial grid with $dx = 0.01$ over $[0, 1]$ for duration $T = 3600$ s using semi-implicit time-stepping with $dt = 300$ s. Dynamics are driven by a localized surface perturbation of amplitude 0.2 at $x = 0.02$, with bottom drag coefficient 0.001, gravitational acceleration $g = 9.81$ m/s², and dry boundary conditions at depth -10 . The Fourier representation emphasizes frequency-localized features informative for depth inference.

B.3. High-Dimensional Bayesian Denoising

The prior $p(\boldsymbol{\theta})$ is defined implicitly over clean images $\boldsymbol{\theta} \in \mathbb{R}^{784}$ (vectorized 28×28 Fashion-MNIST images), i.e., samples of $\boldsymbol{\theta}$ are drawn uniformly from the dataset without assuming a tractable analytical density. The observation model simulates a blurred, photon-limited camera,

$$\mathbf{y} = \alpha \text{Poisson}(\lambda \mathcal{B}_\sigma(\boldsymbol{\theta})), \quad (18)$$

where \mathcal{B}_σ denotes convolution with an isotropic Gaussian kernel of width $\sigma = 2.5$, and $\lambda = 1.0$, $\alpha = 0.5$ control pre- and post-Poisson intensity scaling. This severely ill-posed inverse problem eliminates high frequencies via blur and introduces signal-dependent noise. No labels, side information, or image-specific architectural priors are used ([Radev et al., 2023](#); [Ramesh et al., 2022](#)).

C. Hyperparameters

C.1. Benchmarks Hyperparameters

We tune *OneFlowSBI* separately for each SBIBM task using Optuna (Akiba et al., 2019) (50 trials), selecting the configuration with the lowest validation C2ST. Across tasks, we optimize with Adam (Kingma & Ba, 2014) using $(\beta_1, \beta_2) = (0.9, 0.999)$, gradient clipping at norm 1.0, and exponential moving average (EMA) weights with decay 0.999; EMA parameters are used for evaluation and sampling. We standardize both θ and y using training-set statistics. Unless noted otherwise, we apply a linear learning-rate warmup followed by cosine decay. The task-specific choices are model capacity (hidden dimension and number of residual blocks), peak learning rate, batch size, warmup length, and time sampling (Uniform or U-shaped (Lee et al., 2024)), which are reported in Table 2. All models are trained for 100,000 iterations on a single NVIDIA T4 GPU, using a 90/10 train/validation split with early stopping (patience 20; validation every 500 iterations). For all conditional sampling queries we use adaptive Runge-Kutta solver (DOPRIS5) via `torchdiffeq` (Chen, 2018).

Table 2. **SBIBM hyperparameters:** Task-specific architecture and training settings selected via validation for each benchmark.

Task	Architecture		Optimization			Time sampling
	Hidden dimension	# blocks	Batch size	Peak learning rate	Warmup steps	
Two Moons	200	4	2048	1×10^{-3}	2500	Uniform
Gaussian Mixture	128	3	1024	5×10^{-4}	1500	U-shaped
Gaussian Linear	100	3	1024	5×10^{-4}	1000	Uniform
Gaussian Linear Uniform	128	3	512	1×10^{-3}	2000	Uniform
SIR	256	4	2048	1×10^{-3}	2000	Uniform
SLCP	128	4	2048	5×10^{-4}	5000	U-shaped
SLCP Distractors	256	4	512	1×10^{-4}	2000	U-shaped
Bernoulli GLM	512	4	1024	5×10^{-5}	1000	U-shaped
Bernoulli GLM (raw)	256	4	512	1×10^{-4}	1500	Uniform
Lotka–Volterra	256	4	1024	5×10^{-4}	2000	U-shaped

C.2. Bayesian Image Deblurring Hyperparameters

For Bayesian deblurring, both the prior and the corresponding observation are single-channel 28×28 images. The joint flow vector field takes the noisy joint state $\mathbf{z}_t = (\theta, y)$ as input together with the corresponding observation mask, concatenated into a 4-channel image (two channels for the state and two for the mask) indicating observed (1) and unobserved (0) regions. The vector field is parameterized by a time-conditioned convolutional network consisting of four time-dependent FiLM residual convolutional blocks with 128 hidden channels throughout. Each block uses 3×3 convolutions with stride 1 and padding 1 to preserve spatial resolution, and applies FiLM modulation using a sinusoidal time embedding. A final 3×3 convolution maps the 128-channel features back to 2 output channels, predicting velocities for both θ and y . All other settings, including the masking scheme, follow those used for the SBIBM benchmarks. Training is performed on a budget of 30,000 simulated pairs for 100,000 iterations with batch size 1024 using Adam (learning rate 5×10^{-4}), exponential moving average with decay 0.999, gradient clipping at 1.0, and uniform time sampling.

C.3. Shallow Water Problem Hyperparameters

The prior is defined over basin depth profiles $\theta \in \mathbb{R}^{100}$, with observations $y \in \mathbb{R}^{2 \times 101 \times 100}$ representing Fourier-transformed surface wave fields (real and imaginary components). The architecture uses a dual-stream design: a θ -stream processes the depth profile and mask via a three-layer MLP with 256 hidden units and SiLU activations; a y -stream encodes spatial observations via a CNN with 128 channels, three residual blocks (GroupNorm, kernel size 3), and adaptive average pooling. Feature vectors are concatenated and processed through four AdaLN-conditioned residual blocks with sinusoidal time embeddings. Separate velocity heads predict v_θ (two-layer MLP) and v_y (transposed-convolution decoder); final layers are zero-initialized. The loss applies MSE only on unobserved regions with reweighting factor 200.0 for θ . Training uses 100,000 iterations, batch size 256, Adam optimizer (learning rate 5×10^{-4}), gradient clipping at 1.0 and uniform time sampling.

D. Additional Results

D.1. Posterior visualizations on SBIBM benchmarks

We provide visualizations of the estimated posterior distribution for all ten SBIBM tasks to enable direct inspection of how well *OneFlowSBI* matches the SBIBM reference posterior at the maximum simulation budget (30,000). For each task, we condition on the first SBIBM test observation and draw 10,000 posterior samples from *OneFlowSBI* using the posterior mask. These figures complement the quantitative C2ST comparisons in the main paper by providing a visual check of mode coverage, correlation structure, and tail behaviour across heterogeneous simulators.

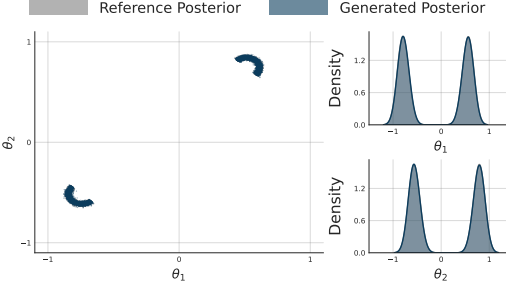


Figure 8. Two Moons. The generated posterior matches the reference crescents and separates the two modes; the one-dimensional marginals over θ_1 and θ_2 closely overlap.

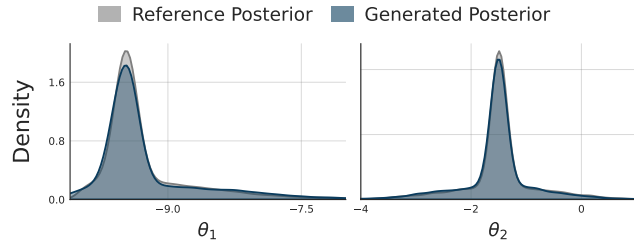


Figure 9. Gaussian Mixture. The generated one-dimensional marginals closely match the reference, capturing the dominant mass and tail behavior in θ_1 and θ_2 .

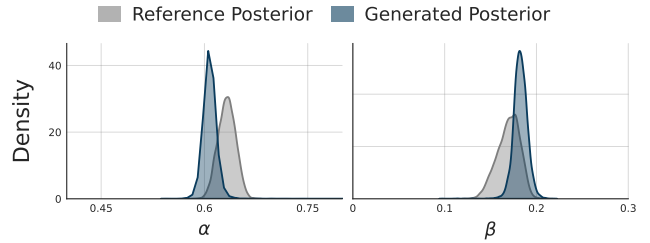


Figure 10. SIR. The generated marginals over α and β align with the reference while showing a small shift in location, indicating mild mismatch under this observation.

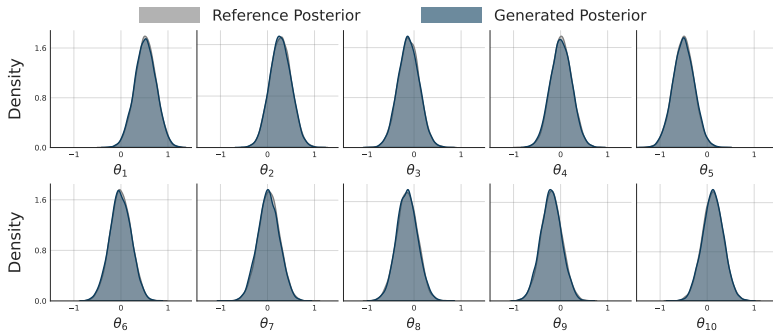


Figure 11. Gaussian Linear. In this conjugate setting, the generated posterior marginals closely match the SBIBM reference across all dimensions, reflecting accurate recovery of the analytic posterior structure.

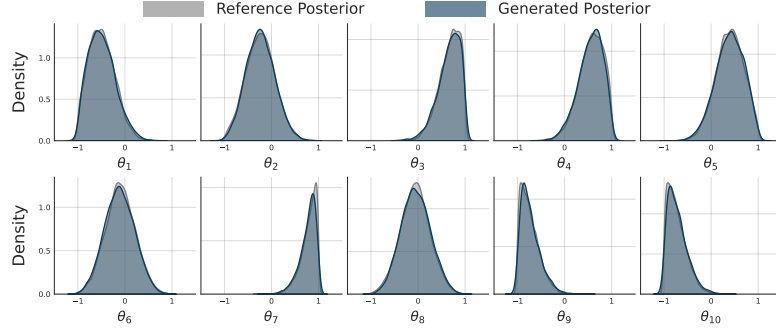


Figure 12. **Gaussian Linear Uniform.** In this non conjugate variant, the generated posterior matches the dominant marginal structure of the SBIBM reference, with mild residual deviations in a few coordinates, most visible in the tails.

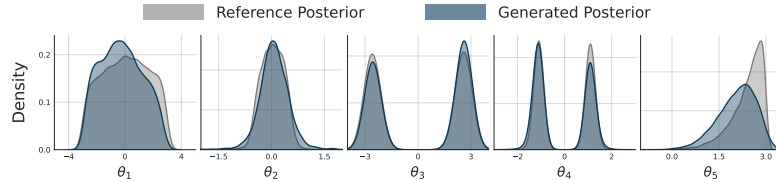


Figure 13. **SLCP.** Generated posterior matches the reference posterior across both unimodal and multi-peaked marginals (e.g., the bimodality in θ_3 and θ_4), capturing the dominant modes and relative mass; remaining mismatch is concentrated in low-density regions and tail behavior (most visibly in θ_5).

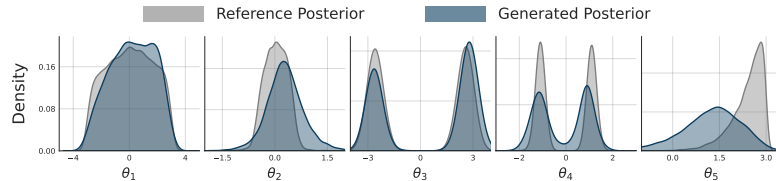


Figure 14. **SLCP Distractors.** For this task, observations are heavily corrupted: out of the 100 observation dimensions, only 8 are informative, while the remaining 92 are distractors drawn from a heavy-tailed mixture and randomly permuted across dimensions. Despite this, *OneFlowSBI* recovers the coarse posterior geometry, including multi-modal marginals; however, because the model learns the full joint distribution, a substantial fraction of training capacity is devoted to capturing irrelevant distractor structure.

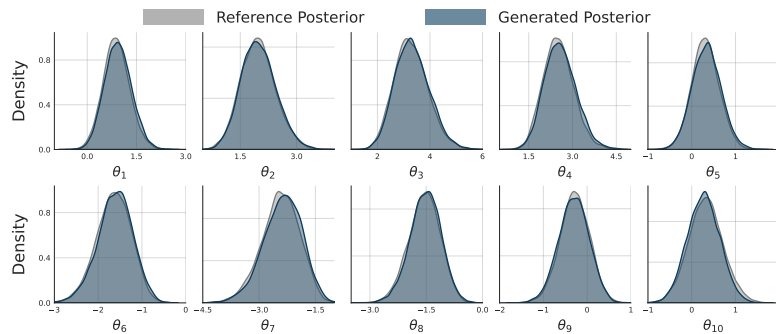


Figure 15. **Bernoulli GLM.** With low-dimensional summary statistics, *OneFlowSBI* closely matches the reference posterior across marginals, preserving concentration and overall dependence structure; small deviations appear as mild over-dispersion in a few coordinates (e.g., slightly broader peaks).

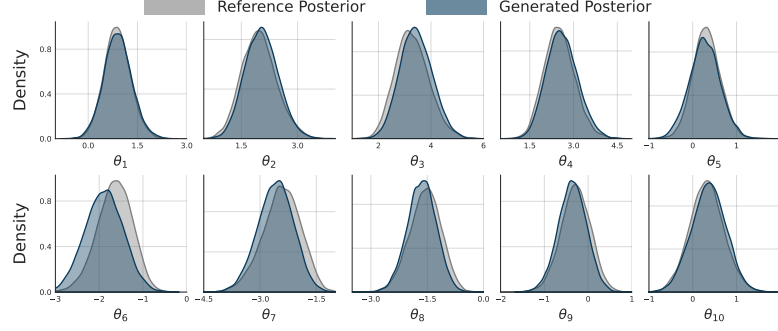


Figure 16. Bernoulli GLM (raw). Conditioning on raw 100-dimensional observations makes inference markedly harder: while the main posterior mass is recovered, several marginals become visibly broader and exhibit increased tail mismatch, consistent with reduced effective signal and a more challenging observation model.

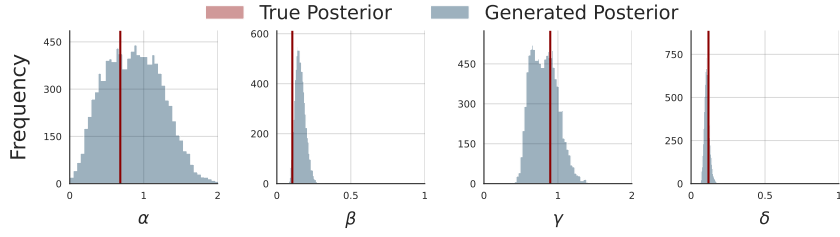


Figure 17. Lotka-Volterra. The reference posterior is extremely concentrated (very small variance), so even minor discrepancies in the learned posterior become visually prominent. This task is challenging due to strong parameter coupling and limited identifiability from the observation, making accurate recovery of such sharp marginals difficult.

D.2. Bayesian Image Deblurring: Additional Results

Posterior Structure Across Image Classes. The posterior structure learned by *OneFlowSBI* for implicit-prior image deblurring is summarized in Figure 18. Across different Fashion-MNIST classes, posterior samples generated from a single blurred and noisy observation preserve class-consistent global structure while exhibiting meaningful variability. The posterior mean recovers the dominant shape of the underlying object despite severe degradation, whereas the posterior standard deviation is spatially structured and concentrates mostly around the boundaries and fine-scale details where the blur operator removes information. These results demonstrate that *OneFlowSBI* captures high-dimensional uncertainty rather than collapsing to over-smoothed point estimates, consistently across diverse image classes.

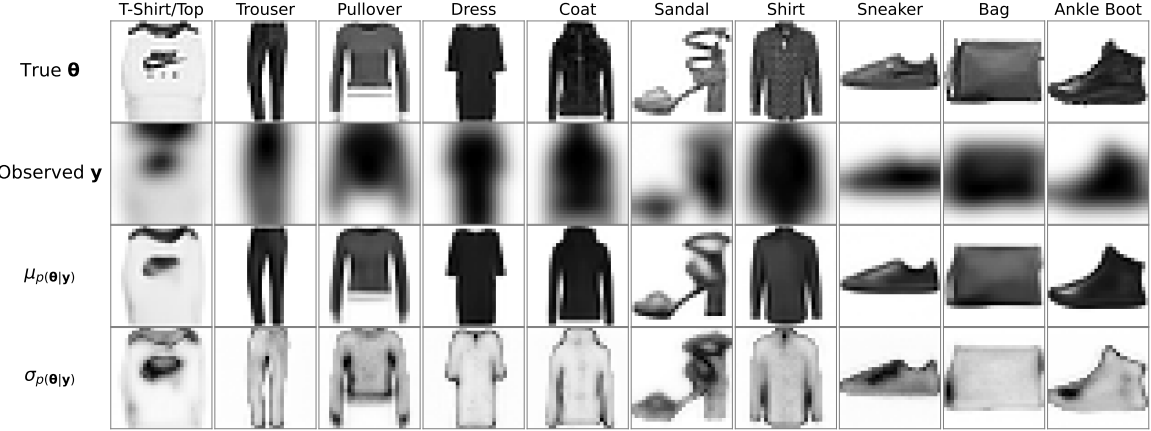


Figure 18. **Bayesian image deblurring.** Posterior mean and standard deviation from 500 samples across different classes, showing accurate class-consistent reconstructions with uncertainty localized to ambiguous regions.

Robustness to Missing Observations. We evaluate robustness to partial observations by randomly masking a 10×10 patch in each input and performing posterior inference conditioned on the remaining pixels. Figure 19 shows that the posterior mean captures coarse, semantically meaningful structure, even though fine details are not fully recovered. The posterior uncertainty is concentrated in the masked regions and their vicinity, indicating increased epistemic uncertainty where information is missing. Overall, these results suggest that *OneFlowSBI* can accommodate missing observations and produce reasonable, uncertainty-aware posterior estimates by leveraging global structure in the learned joint distribution.

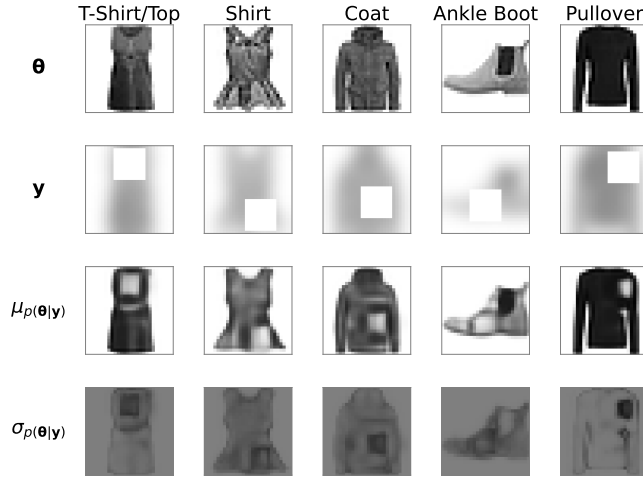


Figure 19. **Posterior inference with missing data.** Posterior mean $\mu_p(\theta | y)$ and standard deviation $\sigma_p(\theta | y)$ estimated from 1000 posterior samples under random masking. While the full structure is not completely recovered, the model produces plausible reconstructions and correctly localizes uncertainty to the masked regions.

NPE Baseline. For comparison, we report results from Neural Posterior Estimation (NPE) (Papamakarios & Murray, 2016), where the posterior is parameterized by a neural spline flow with 100 hidden features. Unlike *OneFlowSBI*, NPE requires an

explicit low-dimensional summary of the observation; here, the noisy image is compressed using a convolutional summary network consisting of four 3×3 Conv2D layers with channel sizes (64, 64, 128, 128), followed by ReLU activations, batch normalization, global average pooling, and a linear projection to a 128-dimensional embedding. The model is trained using the same simulation budget as *OneFlowSBI* with batch size 128 and converges after approximately 155 epochs. Figure 20 shows posterior samples obtained from NPE for a held-out observation. Compared to *OneFlowSBI*, the resulting posterior exhibits weaker spatial coherence and higher uncertainty, particularly around edges and fine-scale structures, consistent with information loss introduced by the learned low-dimensional summary.

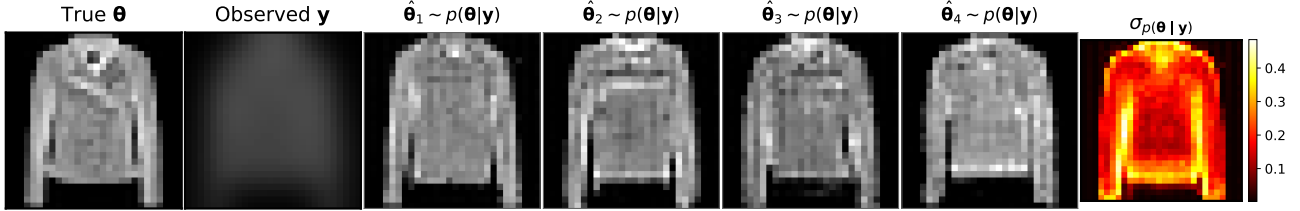


Figure 20. Posterior inference for Bayesian image deblurring (NPE). Posterior samples from NPE exhibit higher uncertainty and reduced spatial coherence compared to *OneFlowSBI*.

D.3. Shallow Water Problem: Additional Results

Robustness to Missing Frequency Information. We evaluate robustness to incomplete observations by conditioning on progressively masked frequency-domain wavefields and examining the induced posterior over basin depth profiles. Figure 21 shows posterior samples for a test instance as the fraction of missing coefficients increases from 0% to 90%. Under mild to moderate missingness (up to 50%), the posterior remains concentrated around the true depth profile, indicating effective information propagation from observed frequencies. As missingness increases (70–90%), uncertainty grows substantially and becomes spatially structured, reflecting genuine non-identifiability rather than numerical artifacts: the posterior mean remains smooth and physically plausible while variability increases in weakly constrained regions. *OneFlowSBI* degrades gracefully under severe information loss by expressing uncertainty through the posterior rather than collapsing to spurious point estimates.

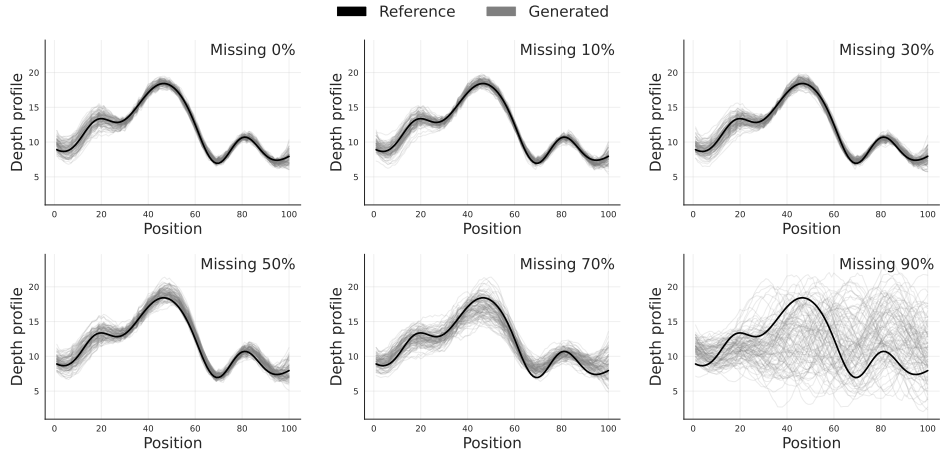


Figure 21. Posterior inference under observation missingness (shallow-water model). Posterior depth samples (gray) and the ground-truth profile (black) for a representative test case, shown for increasing levels of observation missingness from 0% to 90%.

NPE Baseline. For comparison, we train a specialized posterior estimator using Neural Posterior Estimation (NPE) (Papamakarios & Murray, 2016) with a neural spline flow (NSF) containing 128 hidden features. Since observations are high-dimensional ($2 \times 101 \times 100$), the flow is conditioned on a learned embedding rather than raw fields. The embedding network is a spectral-normalized convolutional encoder with five Conv2D layers (kernel size 4): $2 \rightarrow 256$ (stride 1, padding 0), $256 \rightarrow 128$ (stride 2, padding 1), $128 \rightarrow 64$ (stride 2, padding 1), $64 \rightarrow 64$ (stride 2, padding 1), and $64 \rightarrow 1$ (stride 2, padding 1).

1). The first four layers use BatchNorm and ReLU; the final layer uses Tanh activation. The resulting feature map is pooled to 6×6 , flattened, and projected via a spectral-normalized linear layer ($36 \rightarrow 128$) to obtain the conditioning embedding. Training uses batch size 128; evaluation draws 1,000 posterior samples. Figure 22 shows NPE produces more diffuse depth posteriors that deviate from the reference solution, yielding posterior predictive wavefields with increased variability and weaker agreement with observed amplitudes, particularly at later time steps. This highlights the difficulty of posterior-only methods in capturing the strong global parameter–observation coupling in the shallow-water system.

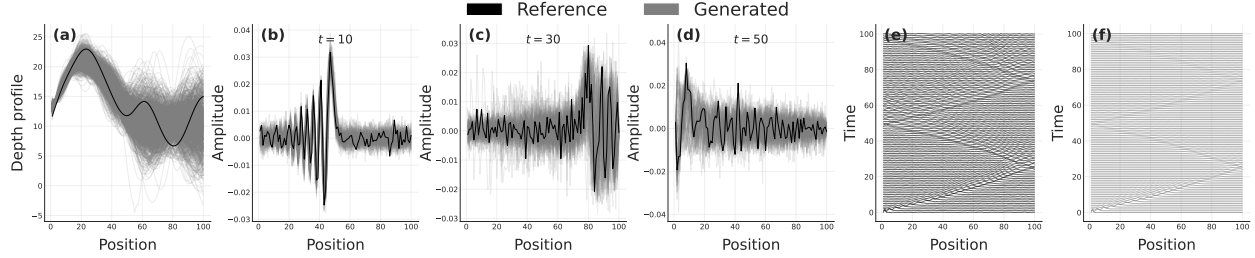


Figure 22. Posterior predictive checks for shallow water using NPE. (a) Posterior samples of the inferred depth profile compared to the ground truth. (b–d) Wave amplitude at selected time steps $t \in \{10, 30, 50\}$, showing posterior predictive draws. (e–f) Full spatiotemporal wavefield reconstructions. Generated samples capture the dominant wave structure but exhibit increased dispersion and phase variability compared to reference simulations.

E. Quantitative posterior metrics on SBIBM

We evaluate posterior quality on all ten SBIBM tasks using C2ST and kernel MMD, comparing *OneFlowSBI* against Simformer (Dense), Simformer (Undirected), and NPE. We report MMD² with a Gaussian kernel using an unbiased estimator and median heuristic for bandwidth selection. The two Simformer variants achieve nearly identical results on low-dimensional tasks (Two Moons and GMM), suggesting that masking directionality has minimal impact in low dimensional regime. For Lotka–Volterra, C2ST saturates at 1.0 for all methods due to extreme posterior concentration (marginal standard deviations $\sim 10^{-4}$). In such near-deterministic regimes, even minor discrepancies make samples trivially separable, reducing C2ST’s discriminative power. We therefore interpret both metrics together, noting that MMD² provides a complementary view but remains sensitive to bandwidth and scale in highly concentrated posteriors (Lueckmann et al., 2021).

Table 3. Posterior C2ST (mean \pm std. over 5 runs and 10 observations) across simulation budgets; best in **bold**, second-best underlined.

Method	SLCP Distractors			Bernoulli GLM (raw)			Lotka–Volterra		
	10k	20k	30k	10k	20k	30k	10k	20k	30k
NPE	<u>0.937</u> ± 0.036	0.909 ± 0.045	0.897 ± 0.049	0.784 ± 0.034	0.729 ± 0.042	<u>0.697</u> ± 0.042	1.000 ± 0.00	1.000 ± 0.00	1.000 ± 0.00
Simformer (Dense)	0.874 ± 0.041	0.837 ± 0.048	0.826 ± 0.045	0.969 ± 0.027	0.870 ± 0.043	0.819 ± 0.043	1.000 ± 0.000	1.000 ± 0.00	1.000 ± 0.00
Simformer (Undirected)	0.979 ± 0.010	0.979 ± 0.010	0.979 ± 0.010	0.998 ± 0.002	0.938 ± 0.041	0.871 ± 0.081	1.000 ± 0.000	1.000 ± 0.00	1.000 ± 0.00
OneFlowSBI	0.966 ± 0.006	<u>0.906</u> ± 0.012	<u>0.883</u> ± 0.011	<u>0.921</u> ± 0.050	<u>0.758</u> ± 0.086	0.653 ± 0.029	1.000 ± 0.000	1.000 ± 0.00	1.000 ± 0.00

Method	Gaussian Mixture			Gaussian Linear			Gaussian Linear Uniform			SLCP		
	10k	20k	30k									
NPE	0.582 ± 0.025	0.545 ± 0.013	0.559 ± 0.056	0.583 ± 0.029	0.555 ± 0.026	0.547 ± 0.023	<u>0.600</u> ± 0.036	<u>0.565</u> ± 0.018	<u>0.561</u> ± 0.024	0.881 ± 0.040	0.850 ± 0.049	0.837 ± 0.056
Simformer (Dense)	<u>0.517</u> ± 0.011	<u>0.510</u> ± 0.007	<u>0.509</u> ± 0.008	0.669 ± 0.061	0.665 ± 0.070	0.611 ± 0.059	0.656 ± 0.057	0.638 ± 0.048	0.622 ± 0.043	<u>0.773</u> ± 0.054	<u>0.710</u> ± 0.050	<u>0.674</u> ± 0.064
Simformer (Undirected)	0.516 ± 0.008	0.509 ± 0.006	0.508 ± 0.006	<u>0.509</u> ± 0.006	0.506 ± 0.004	0.503 ± 0.005	0.514 ± 0.008	0.508 ± 0.006	0.505 ± 0.004	<u>0.637</u> ± 0.060	0.582 ± 0.044	0.569 ± 0.046
OneFlowSBI	0.519 ± 0.004	0.519 ± 0.004	0.511 ± 0.005	<u>0.550</u> ± 0.012	<u>0.518</u> ± 0.004	<u>0.510</u> ± 0.003	0.630 ± 0.010	0.586 ± 0.002	0.566 ± 0.003	0.905 ± 0.014	0.799 ± 0.013	0.735 ± 0.017

Method	Two Moons			Bernoulli GLM			SIR		
	10k	20k	30k	10k	20k	30k	10k	20k	30k
NPE	0.592 ± 0.056	0.581 ± 0.050	0.572 ± 0.052	0.696 ± 0.030	<u>0.635</u> ± 0.027	0.645 ± 0.035	<u>0.824</u> ± 0.128	<u>0.824</u> ± 0.120	<u>0.828</u> ± 0.122
Simformer (Dense)	0.556 ± 0.077	<u>0.514</u> ± 0.013	0.509 ± 0.010	<u>0.661</u> ± 0.038	0.638 ± 0.036	0.624 ± 0.030	0.833 ± 0.123	0.833 ± 0.125	0.831 ± 0.122
Simformer (Undirected)	0.556 ± 0.077	<u>0.514</u> ± 0.013	0.509 ± 0.010	0.640 ± 0.040	0.618 ± 0.032	<u>0.595</u> ± 0.027	0.828 ± 0.121	0.828 ± 0.122	0.833 ± 0.124
OneFlowSBI	0.523 ± 0.004	0.514 ± 0.003	0.512 ± 0.002	0.684 ± 0.049	0.645 ± 0.018	0.579 ± 0.009	0.807 ± 0.009	0.810 ± 0.013	0.810 ± 0.003

Table 4. Posterior MMD² reported as mean \pm std. over 5 runs and 10 observations across simulation budgets; lower is better.

Method	SLCP Distractors			Bernoulli GLM (raw)			Lotka–Volterra		
	10k	20k	30k	10k	20k	30k	10k	20k	30k
NPE	<u>0.110</u> ± 0.052	<u>0.103</u> ± 0.068	<u>0.097</u> ± 0.065	0.117 ± 0.035	0.073 ± 0.051	<u>0.051</u> ± 0.037	0.855 ± 0.339	0.817 ± 0.294	0.795 ± 0.279
Simformer (Dense)	0.099 ± 0.045	0.094 ± 0.057	0.093 ± 0.066	0.416 ± 0.074	0.169 ± 0.048	0.102 ± 0.036	<u>0.574</u> ± 0.048	0.581 ± 0.067	0.575 ± 0.069
Simformer (Undirected)	0.229 ± 0.120	0.228 ± 0.119	0.227 ± 0.119	0.579 ± 0.011	0.392 ± 0.114	0.137 ± 0.088	0.576 ± 0.038	<u>0.574</u> ± 0.048	<u>0.573</u> ± 0.048
OneFlowSBI	0.242 ± 0.046	0.132 ± 0.044	0.110 ± 0.034	<u>0.234</u> ± 0.084	<u>0.082</u> ± 0.060	0.041 ± 0.023	0.567 ± 0.006	0.558 ± 0.010	0.557 ± 0.007

Method	Gaussian Mixture			Gaussian Linear			Gaussian Linear Uniform			SLCP		
	10k	20k	30k	10k	20k	30k	10k	20k	30k	10k	20k	30k
NPE	7.93 ± 0.003	5.45 ± 0.002	5.35 ± 0.002	<u>2.76</u> ± 0.018	1.86 ± 0.001	1.72 ± 0.001	<u>4.09</u> ± 0.002	2.34 ± 0.009	2.25 ± 0.001	<u>0.064</u> ± 0.034	<u>0.042</u> ± 0.025	0.041 ± 0.023
Simformer (Dense)	1.62 ± 0.016	0.30 ± 0.021	0.38 ± 0.029	10.02 ± 0.009	8.15 ± 0.009	5.17 ± 0.006	5.91 ± 0.003	3.86 ± 0.002	3.09 ± 0.001	0.067 ± 0.047	0.044 ± 0.036	<u>0.028</u> ± 0.036
Simformer (Undirected)	0.98 ± 0.001	<u>0.38</u> ± 0.003	<u>0.29</u> ± 0.004	0.24 ± 0.002	0.17 ± 0.001	<u>0.08</u> ± 0.007	0.20 ± 0.001	0.12 ± 0.007	0.11 ± 0.008	0.010 ± 0.013	0.003 ± 0.004	0.005 ± 0.006
OneFlowSBI	1.26 ± 0.004	0.53 ± 0.003	0.30 ± 0.001	3.41 ± 0.011	<u>0.96</u> ± 0.008	<u>0.58</u> ± 0.005	6.23 ± 0.029	1.43 ± 0.002	<u>0.86</u> ± 0.017	0.180 ± 0.022	0.095 ± 0.011	0.040 ± 0.013

Method	Two Moons			Bernoulli GLM			SIR		
	10k	20k	30k	10k	20k	30k	10k	20k	30k
NPE	1.26 ± 0.005	1.14 ± 0.001	1.38 ± 0.005	56.62 ± 0.029	25.52 ± 0.015	34.64 ± 0.023	<u>0.376</u> ± 0.224	<u>0.381</u> ± 0.209	<u>0.379</u> ± 0.215
Simformer (Dense)	<u>1.25</u> ± 0.001	<u>0.40</u> ± 0.007	<u>0.24</u> ± 0.001	<u>28.58</u> ± 0.024	18.54 ± 0.014	16.73 ± 0.0163	0.411 ± 0.225	0.416 ± 0.217	0.411 ± 0.213
Simformer (Undirected)	<u>1.25</u> ± 0.001	0.51 ± 0.007	<u>0.24</u> ± 0.001	29.47 ± 0.024	<u>17.18</u> ± 0.014	<u>10.64</u> ± 0.009	0.405 ± 0.227	0.407 ± 0.215	0.409 ± 0.216
OneFlowSBI	1.06 ± 0.005	0.39 ± 0.003	0.22 ± 0.002	25.30 ± 0.008	16.70 ± 0.002	9.05 ± 0.002	0.344 ± 0.019	0.344 ± 0.026	0.359 ± 0.018

Note: For readability, MMD mean values for the Gaussian Mixture, Gaussian Linear, Gaussian Linear Uniform, Two Moons, and Bernoulli GLM tasks are reported on a scale of 10^{-3} .